Supporting Information

Direct structural and mechanistic insights into fast bimolecular chemical reactions in solution through a coupled XAS/UV–Vis multivariate statistical analysis

Francesco Tavani,[a,*] Giorgio Capocasa,[a] Andrea Martini,[b,c] Francesco Sessa,[a] Stefano Di Stefano,[a] Osvaldo Lanzalunga[a] and Paola D'Angelo[a,*]

[a] Dipartimento di Chimica, Università di Roma "La Sapienza", P.le A. Moro 5, 00185 Roma, Italy.

[b] Dipartimento di Chimica, Università degli Studi di Torino, Via P. Giuria 7, 10125 Torino, Italy.

[c] The Smart Materials Research Institute, Southern Federal University, 344090 Sladkova 178/24 Rostov-on-Don, Russia.

[*] p.dangelo@uniroma1.it, francesco.tavani@uniroma1.it

Materials

All reagents and solvents were employed at the highest commercial quality and were used without further purification. Peracetic acid (36–40 wt% in acetic acid, stored at 4 °C) was acquired from Sigma Aldrich. Fe^{II} bis(trifluoromethanesulfonate) from now on referred to as $Fe(OTf)_2$ was obtained from Strem Chemicals. The N4Py ligand (N4Py = *N*,*N*-bis(2-pyridylmethyl)-*N*-bis(2-pyridyl)methylamine) was prepared following a previously reported procedure,[1] and metalated to yield $[N4Py{\cdot}Fe^{II}(CH_3CN)](OTf)_2$ according to a literature protocol.[2] Preparation and handling of air sensitive materials were carried out under an inert atmosphere by using either Schlenk

and vacuum line techniques or a glove bag under N_2 atmosphere. The complex was then stored under inert atmosphere.[3]

Methods

Monitoring of the reactions between $[N4Py{\cdot}Fe^{IV}(O)]^{2+}$ and the substrates.

Because a pre–mixing cell was not available in the stopped–flow apparatus the $[N4Py{\cdot}Fe^{IV}(O)]^{2+}$ solution was prepared in a vial immediately before the execution of the experiment. 1 mL of a 25 mM stock acetonitrile solution of $[N4Py{\cdot}Fe^{II}](OTf)_2$ was reacted with a solution prepared from 52 μL of a 36–40% w/w solution of peroxyacetic acid in acetic acid (10 eq.) and 200 μL of CH_3CN to afford a 19.9 mM solution of $[N4Py{\cdot}Fe^{IV}(O)]^{2+}$ which was loaded as is in the first syringe of the stopped-flow apparatus. The relatively fast decomposition of the $[N4Py{\cdot}Fe^{IV}(O)]^{2+}$ complex at a 20 mM concentration compared to experimental timescales made it necessary to employ more than a stochiometric amount of oxidant. A solution of the substrate (concentrations equal to 100 mM and to 800 mM for *p*–methoxythioanisole and *p*–cyanothioanisole, respectively) was loaded in the second syringe of the stopped–flow apparatus. The $[N4Py{\cdot}Fe^{IV}(O)]^{2+}$ species and the given substrate were then shot in the stopped–flow apparatus in a 3.5:1.0 volume ratio at room temperature in order to attain the final concentration of 15 mM for the $[N4Py{\cdot}Fe^{IV}(O)]^{2+}$ complex and the desired concentration of substrate.[3]

Energy Dispersive X-ray Absorption and UV–Vis measurements.

Simultaneous EDXAS and UV–Vis spectra were collected at the ID24 beamline of the European Synchrotron Radiation Facility ESRF, Grenoble (the ring energy was 6.0 GeV and the current 150-200 mA).[4] The X-ray source consists of two undulators whose gaps were tuned to place the first harmonic at 7100 eV. The beam was focused horizontally to an 8 μm full width at half maximum (FWHM) spot on the sample by the curved Si(111) polychromator crystal in Bragg geometry. In the vertical direction, the beam was focused using a bent Si mirror at a glancing angle of 3 mrad with respect to the direct beam. To minimize sample radiation damage, the vertical spot

size was set at 40 μm FWHM. Spectra were recorded in transmission mode using a FReLoN (fast read out low noise) high frame-rate detector based on charge coupled device (CCD) cameras optically coupled with a scintillator screen. Acquisition time was 100 ms and 1.8 s for each spectrum for the reactions involving the *p*–methoxythioanisole and *p*–cyanothioanisole substrates, respectively. Sequences of 50-100 individual spectra were acquired and each sequence was repeted three times, and the data were averaged to obtain a better S/N ratio. The energy calibration was made by measuring the absorption spectrum of an iron foil and the first inflection point was set at 7111 eV. All measurements were carried out at 25°C. Simultaneous EDXAS and UV–Vis spectra were recorded with a Bio-Logic SFM-400 stopped-flow device equipped with a flow-through quartz capillary cell. The quartz capillary cell had a diameter of 1.3 mm and wall thickness of about 10 μm. The dead time of the stopped-flow device is about 2.0 ms for the flow rate of 8 ml/s and it defines the shortest kinetic time that is accessible for spectroscopy measurements. However, for the measurements reported here, the stopped-flow device was triggered by the EDXAS data acquisition system. Therefore, the overhead corresponding to the movement of the syringe motors needs to be considered and the kinetic time starts to evolve 96 ms after the trigger was sent. Therefore, the first UV–Vis spectrum is recorded at the beginning of the reaction (t=0 ms) whereas the first EDXAS spectrum is recorded 24 ms after the reaction starts. From this time on EDXAS and UV–Vis data collection is synchronized.

EDXAS data treatment

The stopped-flow apparatus used to carry out the reaction requires a quartz capillary cell that worsens the EDXAS spectra due to scattering by quartz. For each measurement the EDXAS spectrum of the cell containing pure acetonitrile was collected after the sample spectrum, using the same statistic. The cell spectrum was subtracted from the sample spectrum to gain a better S/N ratio, a higher resolution for the structural oscillations and a more defined Fe K-edge position. The spectra were then subjected to a smoothing procedure using the Savitzky-Golay smoothing filter.[5,6] The resulting EDXAS spectra relative to the investigated reactions are shown in Figure S1.

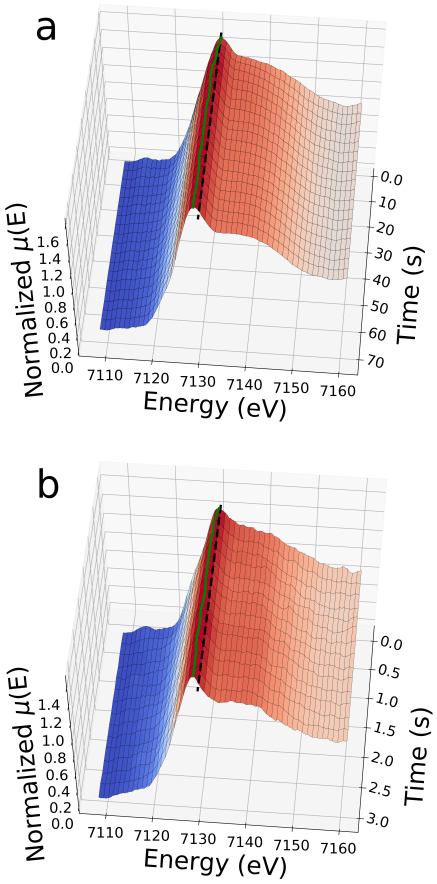

Figure S1: Time evolution of the Fe K-edge EDXAS spectra of the oxidations of *p*–$CNC_6H_4SCH_3$ (a) and *p*–$CH_3OC_6H_4SCH_3$ (b) by $[N4Py{\cdot}Fe^{IV}(O)]^{2+}$ in CH_3CN at 25 °C. A constant energy cut (black, dotted line) is drawn from the absorbance maximum of the first EDXAS spectrum. The shift of the spectra towards lower energies as the reaction proceeds due to the Fe^{IV} reduction is evidenced by the deviation of the EDXAS maxima (green, full line) from the dotted black line.

Decomposition of UV–Vis and EDXAS data into the spectra and fractional concentrations of key components

A large quantity of data is produced by spectroscopical time-resolved measurements. The experimental spectra may be arranged in a spectral matrix

$\boldsymbol{D}$, where each column of $\boldsymbol{D}$ is a spectrum measured at time t. Every measured spectrum may be seen as due to the coexistence of a number N of "pure" and uncorrelated components multiplied by their relative concentration, in accordance with the Lambert-Beer's law.[7] Achieving the decomposition of the experimental spectroscopic dataset into the N spectra associated to the key reaction species and their relative concentration profiles can offer unique comprehension of the reactive process. In the present work, such decomposition was performed with the PyFitit code.[7] To do so, this software employs a strategy belonging to the class of the MCR methods.
The starting point is the Singular Value Decomposition (SVD) expression:

$$\boldsymbol{D} = \boldsymbol{U} \cdot \boldsymbol{\Sigma} \cdot \boldsymbol{V} + \boldsymbol{E} \tag{1}$$

where the product $\boldsymbol{U} \cdot \boldsymbol{\Sigma}$ contains, on its N columns, a set of values that may be associated to the normalized absorption coefficients, $\boldsymbol{\Sigma}$ is a diagonal matrix known as the *singular values* term, whose elements are sorted in decreasing order, while $\boldsymbol{V}$ can be interpreted as the concentration matrix associated to the N-selected components. Lastly, the error matrix $\boldsymbol{E}$ represents the lack of fit between the experimental data matrix $\boldsymbol{D}$ and the reconstructed matrix $\boldsymbol{\mu} = \boldsymbol{U} \cdot \boldsymbol{\Sigma} \cdot \boldsymbol{V}$. The possibility of retrieving from Equation (1) a set of spectra and concentration profiles having a spectroscopic meaning depends on the number of N components present in the experimental data matrix.This may be achieved by combining different statistical tests (further discussed in the following Section) and empirical evidences.[7] Among them, in this work we chose to use the Scree plot and imbedded–error function analyses since they are readily interpreted.
At this point, all matrices in Equation (1) are solely mathematical solutions to the decomposition problem without physico-chemical meaning. Once N is established, the approach implemented by PyFitIt requires the introduction of a transformation N × N matrix $\boldsymbol{T}$ in Equation (1), using the relation $\boldsymbol{I} = \boldsymbol{T} \cdot \boldsymbol{T}^{-1}$:

$$\boldsymbol{D} = \boldsymbol{U} \cdot \boldsymbol{\Sigma} \cdot \boldsymbol{T} \cdot \boldsymbol{T}^{-1} \cdot \boldsymbol{V} + \boldsymbol{E} \tag{2}$$

where the spectra belonging to the key reaction species are given by $\boldsymbol{S} = \boldsymbol{U} \cdot \boldsymbol{\Sigma} \cdot \boldsymbol{T}$ and their concentration profiles by $\boldsymbol{C} = \boldsymbol{T}^{-1} \cdot \boldsymbol{V}$. Subsequently, the matrix elements T_{ij} of matrix $\boldsymbol{T}$ are modified by sliders to achieve $\boldsymbol{S}$ and $\boldsymbol{C}$ which are chemically and physically interpretable. Once this step is achieved, one can finally write:

$$\boldsymbol{D} = \boldsymbol{S} \cdot \boldsymbol{C} + \boldsymbol{E} \tag{3}$$

The unknown number of T_{ij} elements of $\boldsymbol{T}$ is in principle equal to N^2. In order to reduce such ambiguity, some constraints were imposed. In the case of the analyses of the UV–Vis data for both reactions, the transformation matrix elements were varied in order to extract spectral components in accord with known spectra belonging to the reaction species. In the range between 513 nm and 1000 nm the UV–Vis spectrum of complex $[\mathrm{N4Py{\cdot}Fe}^{IV}\mathrm{(O)}]^{2+}$ is constituted by a broad peak centered at approximately $\lambda = 695$ nm. In that same spectral range, the UV–Vis spectrum of complex $[\mathrm{N4Py{\cdot}Fe}^{II}\mathrm{(CH_3CN)}]^{2+}$ is comprised of the shoulder of a transition centered at $\lambda = 495$ nm. The spectra of these two species are shown in Figure S2. Lastly, complex $[\mathrm{N4Py{\cdot}Fe}^{III}\mathrm{(OH)}]^{2+}$, exhibits a very weak absorbance in this spectral range, as evidenced by measurements of time–resolved UV–Vis spectra relative to the activation reactions of a variety of C–H bond containing substrates by $[\mathrm{N4Py{\cdot}Fe}^{IV}\mathrm{(O)}]^{2+}$, which did not reveal an appreciable absorbance by the Fe^{III}–OH intermediate.[2]

In the case of the *p*–$\mathrm{CNC_6H_4SCH_3}$ reaction, a 2×2 matrix $\boldsymbol{T}^1$ was defined containing four variable T^1_{ij} elements. The solution for the decomposition presented in Equation (3) was obtained using the following matrix:

$$\boldsymbol{T}^1 = \begin{pmatrix} -0.281 & -0.275 \\ +0.158 & -1.884 \end{pmatrix} \tag{4}$$

Conversely, the following 3×3 matrix $\boldsymbol{T}^2$ was defined, containing nine T^2_{ij} elements, to decompose the UV–Vis data relative to the *p*–$\mathrm{CH_3OC_6H_4SCH_3}$ reaction:

$$\boldsymbol{T}^2 = \begin{pmatrix} -0.210 & -0.080 & -0.215 \\ -0.985 & -0.235 & +0.120 \\ +0.505 & -0.875 & +0.175 \end{pmatrix} \tag{5}$$

In the case of the decomposition of the EDXAS dataset relative to the *p*–$\mathrm{CH_3OC_6H_4SCH_3}$ oxidation, the normalization of all spectral components contained in matrix $\boldsymbol{S}$ was required. This procedure allows one to reduce the unknown number of the transformation matrix elements from N^2 to $N^2 - N$. Additionally, the experimental EDXAS spectrum measured at t = 3.0 s was fixed to coincide with the third extracted spectral component. This procedure assures a more limited variability in the determination of the unknown T^3_{ij} elements (whose number reduced from nine to four) and was motivated

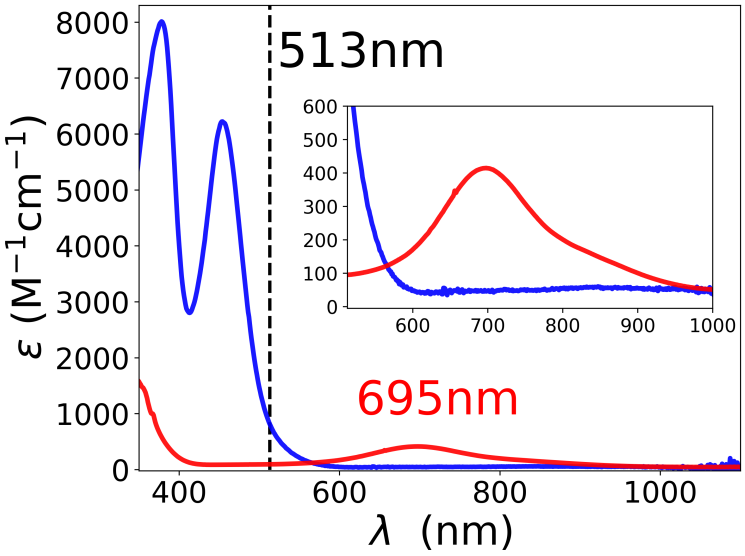

Figure S2: UV–Vis spectra of [N4Py·Fe^{II}(CH$_3$CN)]$^{2+}$ $5.27 \cdot 10^{-5}$ M (a) and [N4Py·Fe^{IV}(O)]$^{2+}$ $1.3 \cdot 10^{-3}$ M (b) in CH$_3$CN at 25°C (optical path: 1 cm). The lower limit of the measured wavelengths (513 nm) is evidenced by a vertical dotted line, and the wavelength in proximity of the absorbance maximum of the Fe^{IV} complex is indicated.

by the fact that no variation in the EDXAS experimental spectra or in the energy position in the main absorption edge is seen after t = 3.0 s.[3] The solution for the decomposition was obtained using the following
3×3 matrix $\boldsymbol{T}^3$:

$$\boldsymbol{T}^3 = \begin{pmatrix} 1/\sigma & 1/\sigma & 1/\sigma \\ 0.7 & 0.2 & T^3_{23} \\ 0.5 & -1.2 & T^3_{33} \end{pmatrix} \tag{6}$$

where σ is the normalization coefficient, while T^3_{23} and T^3_{33} were fixed by constraining the third component ($\sigma = -0.183$, $T^3_{23} = -0.136$, $T^3_{33} = 0.135$).
For all analyses the non-negativity of both UV–Vis and XANES extracted spectral and concentration profiles was implemented by looking for a set of parameters T_{ij} capable of furnishing absorption and concentration profiles that were non-negative.[7,8] For the detailed explanation of how these constraints are imposed, see Ref. 7.

Pseudo–first–order best–fitting of the UV–Vis extracted concentration profiles relative to the oxidation of *p*–$CNC_6H_4SCH_3$

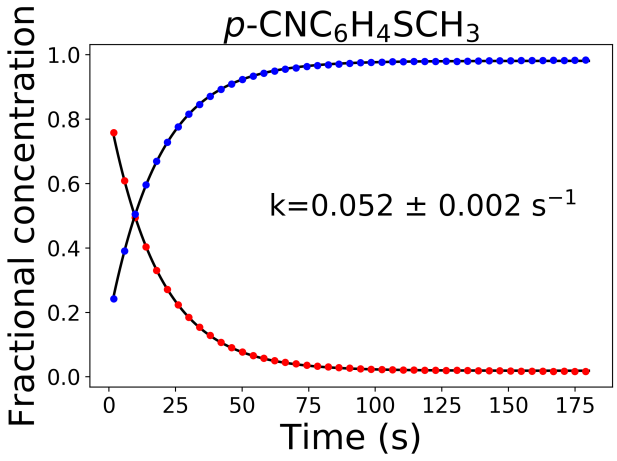

Figure S3: Exponential fit (black solid line) of the concentration profiles extracted from the UV–Vis data of the *p*–$CNC_6H_4SCH_3$ oxidation and assigned to complexes $[N4Py{\cdot}Fe^{II}(CH_3CN)]^{2+}$ and $[N4Py{\cdot}Fe^{IV}(O)]^{2+}$ (selected points are shown as blue and red dotted lines, respectively). The obtained pseudo–first–order kinetic constant is $k = 0.052 \pm 0.002\ s^{-1}$.

Determination of the number of principal components through statistical criteria: Scree plot and IE factor analysis

The UV–Vis spectroscopic data recorded during the reactions of p–$CNC_6H_4SCH_3$ and p–$CH_3OC_6H_4SCH_3$ with $[N4Py{\cdot}Fe^{IV}(O)]^{2+}$ were subjected to the Scree plot and Imbedded Error (IE) factor analyses to determine the number of pure species present in the reaction mixtures. The UV–Vis data were used in opposition to the EDXAS data for the statistical investigation due to their lower degree of experimental noise. The elements of the diagonal matrix $\mathbf{\Sigma}$ in Equation (1) are the singular values σ_{ii} extracted by the SVD procedure. One may show that the following expression holds:

$$s_i = \frac{\sigma_{ii}^2}{m-1} \tag{7}$$

where s_i are the eigenvalues of the covariance matrix of $\boldsymbol{D}$ (evaluated for m energy steps) and correspond to the variance represented by each principal component (PC).[7,9] Therefore, the components characterized by a large σ_{ii} value will contribute in a significant way to the reconstruction of the dataset, while those with a small σ_{ii} value will be associated to statistical noise. Both the Scree plot and the IE function tests rely on the variance values obtained from Equation (7).

In the Scree plot analysis, the singular values relative to each PC are plotted against the number of PCs and the identification of an elbow in the resulting curve marks the distinction between signal and noise related components. Conversely, the IE function is given by:

$$IE = \sqrt{\frac{h\sum_{i=h+1}^{n} s_i}{mn(n-h)}} \tag{8}$$

where h is the number of PCs used for the representation of $\boldsymbol{D}$ and n is the number of time steps in the time-resolved experiment. It can be shown that if the experimental errors are uniformly and randomly distributed for every spectrum of the dataset $\boldsymbol{D}$, then all secondary PCs possess eigenvalues that are approximately the same.[7,9] This finding leads to the possibility of rewriting Equation (8), for $h > N$, as:

$$IE = n^{\frac{1}{2}} \cdot k \tag{9}$$

where k is a constant proportional to the magnitude of the secondary eigenvalues. Therefore, for $h < N$ one may see from Equation (8) that the IE function decreases as the number of PCs increases, whereas for $h > N$ the IE function increases as a function of the number of PCs. This implies that a minimum value is reached at $h = N$.

Analysis of the Fe K–edge low–energy region

The identification of the energy position of the single-hole transitions is not an easy task due to the superposition of bound transitions that appear as shoulders on the X-ray absorption edges. The energy of the absorption edge is usually defined as the first inflection point of the spectrum. However, the presence of transitions to bound states usually affects the shape of the edge and it is therefore not easy to determine such an inflection point. To overcome this problem an accurate determination of the edge position of the Fe K–edge XANES spectra obtained from our analysis has been performed by deconvolving the threshold region of the spectra as a sum of an arctangent function describing the transition into the continuum, and a Lorentzian function representing the 1s→4s transition. The two functions have been convoluted with a Gaussian function accounting for the experimental resolution. The deconvolution procedure has been performed using a least-squares fitting scheme on the threshold region of the normalized spectra. The results of the minimization procedures for the Fe K-edge extracted XANES spectra of the key iron species relative to the oxidations of *p*–$CNC_6H_4SCH_3$ and *p*–$CH_3OC_6H_4SCH_3$ by $[N4Py{\cdot}Fe^{IV}(O)]^{2+}$ are shown in Figures S4 and S5, respectively.

The threshold energies obtained from this procedure are listed in Table S1 together with approximate energy values of the pre–edge peaks for the extracted Fe K–edge spectra.

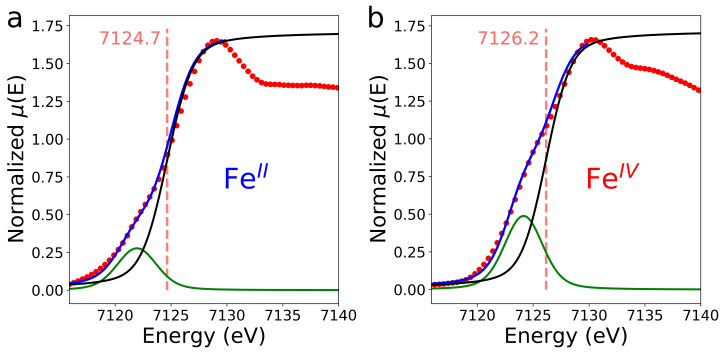

Figure S4: Deconvolution of the extracted XANES spectra of the key iron species relative to the oxidation of *p*–$CNC_6H_4SCH_3$ by $[N4Py{\cdot}Fe^{IV}(O)]^{2+}$. The extracted spectra (red dots) have been fitted using the convolution of a Lorentzian function (green line) representing the 1s→4s transition and an arctangent function (black line) describing the transition into the continuum. Within each spectrum the dashed line locates the arctangent inflection point whose energy value is reported.

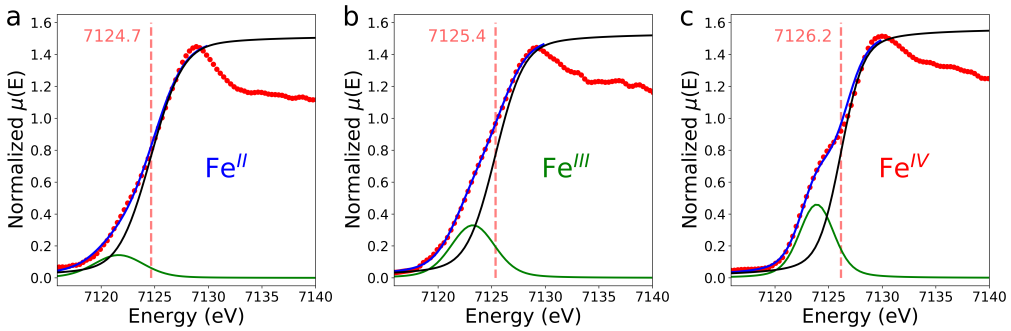

Figure S5: Deconvolution of the extracted XANES spectra of the key iron species relative to the oxidation of *p*–$CH_3OC_6H_4SCH_3$ by $[N4Py{\cdot}Fe^{IV}(O)]^{2+}$. The extracted spectra (red dots) have been fitted using the convolution of a Lorentzian function (green line) representing the 1s→4s transition and an arctangent function (black line) describing the transition into the continuum. Within each spectrum the dashed line locates the arctangent inflection point whose energy value is reported.

	$E_0(eV)$	$E_{pre-edge}(eV)$
Fe^{IV}		
Rohde et al.[10]	7123.6	7114.3
Chandrasekaran et al.[11]	-	7113.6
This work	7126.2	7113.3(2)
Fe^{III}		
Rohde et al.[10]	7123.4	7113.5
This work	7125.4	7112.4(2)
Fe^{II}		
Rohde et al.[10]	7122.0	7112.9
This work	7124.7	7111.8(2)

Table S1: Experimental energies for the Fe K–edge main absorption edges (E_0) and for the pre–edge peaks ($E_{pre-edge}$) for the Fe^{IV}, Fe^{III} and Fe^{II} key species determined in the present investigation as compared to the literature values.

XANES data analysis

Each XANES spectral component extracted from the decomposition of the EDXAS data relative to the oxidation of *p*–$CH_3OC_6H_4SCH_3$ and *p*–$CNC_6H_4SCH_3$ by $[N4Py{\cdot}Fe^{IV}(O)]^{2+}$ was assigned to a reaction key species and analyzed using the MXAN code.[12–14] This code is based on the calculation of theoretical spectra with a multiple scattering (MS) approach in the framework of the muffin tin (MT) approximation using a complex optical potential, based on the local density approximation of the excited photoelectron self-energy.[15–17] The MT radii have been calculated according to the Norman criterion. The self-energy is calculated in the framework of the Hedin-Lundqvist

(HL) scheme using only the real part of the HL potential while an empirical approach is employed to account for inelastic losses in which the plasmon amplitude, A_s and the energy onset, E_s are refined.[18] In all analyses the core hole lifetime Γ_c was kept fixed at 1.25 eV for Fe, while the experimental resolution Γ_{exp} was optimized during the minimization procedure using a Gaussian function.

The analysis of the XANES spectrum assigned to the species $[\text{N4Py}\cdot\text{Fe}^{II}(\text{CH}_3\text{CN})]^{2+}$ has been carried out starting from an octahedral coordination model around the Fe atoms based on the crystallographic structure of the same complex.[19] In this structure the Fe photoabsorber is coordinated by four nitrogen atoms belonging to the N4Py pyridine rings (N_{Py}), by one nitrogen atom bound to three carbon atoms (N_{amine}) and by a CH_3CN solvent nitrogen atom (N_{ACN}). The minimization procedures relative to the Fe^{II} species has been carried out by optimizing the Fe–N_{Py} four distances, the Fe–N_{amine} and the Fe–N_{ACN} single distances. The orientation of the CH_3CN molecule was optimized within a preset range of $\pm 30°$ around the initial structure, whereas the orientation of the rest of the molecule was optimized within $\pm 1°$.

The XANES calculations regarding complex $[\text{N4Py}\cdot\text{Fe}^{IV}(\text{O})]^{2+}$ were based on the previously reported X-ray cristallography molecular structure.[20] In this complex, the central metal cation is coordinated to the four N4Py pyridine nitrogen atoms, to the N_{amine} nitrogen atom and to an oxygen atom. The minimization procedure was applied by optimizing all the Fe–N_{Py}, Fe–N_{amine} and the Fe–O distances independently. The orientation of the oxygen atom and of the rest of the molecule was optimized within a preset range of $\pm 30°$ and $\pm 2°$ around the initial structure, respectively. All the mentioned Fe–ligand distances relative to the Fe^{II} and Fe^{IV} complexes were allowed to vary within ± 0.05 Å of the crystallographic ones.

The MS analysis of $[\text{N4Py}\cdot\text{Fe}^{III}(\text{OH})]^{2+}$ has been carried out starting from the crystallographic structure of complex $[\text{N4Py}\cdot\text{Fe}^{IV}(\text{O})]^{2+}$. Also in this case, all the Fe–N_{Py}, Fe–N_{amine} and the Fe–O distances were independently refined. The orientation of the oxygen atom and of the rest of the molecule were minimized within a preset range of $\pm 27°$ and $\pm 3°$ around the initial structure, respectively. During the minimization procedures of the Fe^{IV}, Fe^{II} and Fe^{III} complexes all the carbon atoms belonging to the molecular structures were linked as rigid bodies to the respective nearest nitrogen ligand, and the relative positions between them, the given nitrogen ligand, and the other carbon atoms constrained to the same nitrogen ligand were conserved. Hydrogen atoms have not been included in all MXAN analyses. For

all spectra, five nonstructural parameters have been optimized, namely, the difference between the theoretical threshold energy and the first inflection point of the spectrum, E_T, the Fermi energy level, E_F, the energy and amplitude of the plasmon, E_s and A_s, and the experimental resolution Γ_{exp}. The quality of the fits has been estimated with the residual function, R_{sq}.[12–15] The comparison of the XANES calculations for the Fe^{IV} and Fe^{II} species with the extracted spectral components from the EDXAS data relative to the *p*–$CNC_6H_4SCH_3$ oxidation and assigned to the same complexes is shown below in Figure S6.

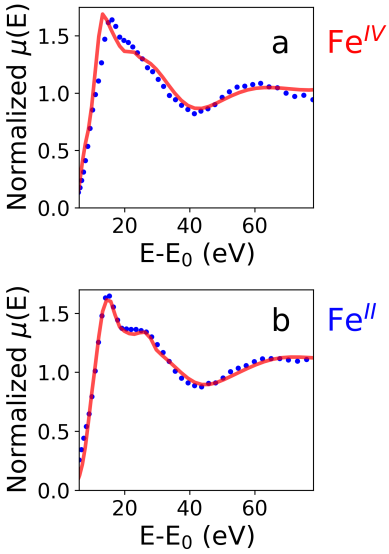

Figure S6: (a) Comparison between the XANES best–fit theoretical spectrum of the $[N4Py{\cdot}Fe^{IV}(O)]^{2+}$ complex (red) and the associated experimental XANES component obtained from the deconvolution of the time–resolved EDXAS data relative to the *p*–$CNC_6H_4SCH_3$ oxidation (black). (b) Comparison between the XANES best–fit theoretical spectrum of the $[N4Py{\cdot}Fe^{II}(CH_3CN)]^{2+}$ complex (red) and the associated experimental XANES component obtained from the deconvolution of the time–resolved EDXAS data relative to the *p*–$CNC_6H_4SCH_3$ oxidation (black).

Kinetic analysis

The concentration profiles for the reaction species extracted by decomposing the EDXAS data for the *p*–$CH_3OC_6H_4SCH_3$ oxidation were analyzed with the Odenlls Python3 library to extract kinetic information.[21] Because of the pseudo–first–order experimental conditions, the assumed model for the reaction was $Fe^{IV} \overset{k_1}{\Rightarrow} Fe^{III} \overset{k_2}{\Rightarrow} Fe^{II}$, with the associated coupled differential equations:

$$\begin{cases} \frac{d[Fe^{IV}]}{dt} = -k_1 \cdot [Fe^{IV}] \\ \frac{d[Fe^{III}]}{dt} = +k_1 \cdot [Fe^{IV}] - k_2 \cdot [Fe^{III}] \\ \frac{d[Fe^{II}]}{dt} = +k_2 \cdot [Fe^{III}] \end{cases} \tag{10}$$

The obtained solutions were simultaneously fitted to the EDXAS-extracted concentration profiles. The residuals associated to the best–fit obtained solution are shown in Figure S7. The R^2 value is 0.985.

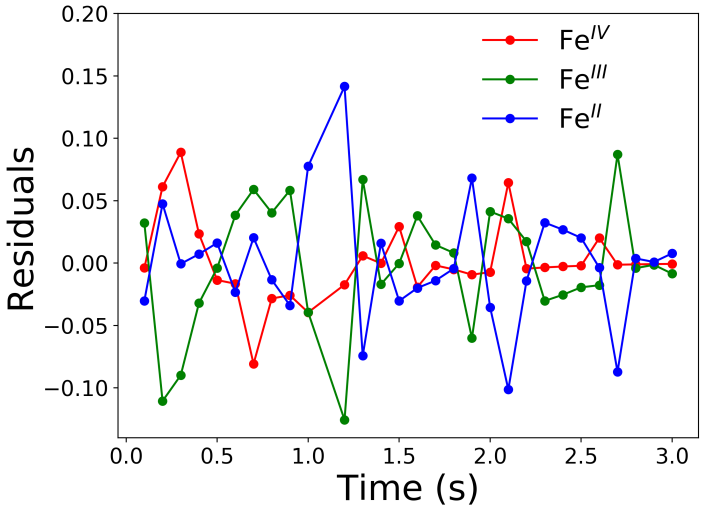

Figure S7: Residual differences between the EDXAS-extracted concentration profiles for the *p*–$CH_3OC_6H_4SCH_3$ oxidation and those estimated by the kinetic fit.

References

[1] M. Lubben, A. Meetsma, E. C. Wilkinson, B. Feringa and L. Que Jr., *Angew. Chem. Int. Ed.*, 1995, **34**, 1512–1514.

[2] K.-B. Cho, X. Wu, Y.-M. Lee, Y. H. Kwon, S. Shaik and W. Nam, *J. Am. Chem. Soc.*, 2012, **134**, 20222–20225.

[3] G. Capocasa, F. Sessa, F. Tavani, M. Monte, G. Olivo, S. Pascarelli, O. Lanzalunga, S. Di Stefano and P. D'Angelo, *J. Am. Chem. Soc.*, 2019, **141**, 2299–2304.

[4] S. Pascarelli, O. Mathon, T. Mairs, I. Kantor, G. Agostini, C. Strohm, S. Pasternak, F. Perrin, G. Berruyer, P. Chappelet, C. Clavel and M. C. Dominguez, *J. Synchr. Rad.*, 2016, **23**, 353–368.

[5] W. H. Press, S. a. Teukolsky, W. T. Vetterling and B. P. Flannery, *Numerical Recipes in Fortran 77: the Art of Scientific Computing. Second Edition*, 1996, vol. 1.

[6] P. A. Gorry, *Anal. Chem.*, 1990, **62**, 570–573.

[7] A. Martini, S. Guda, A. Guda, G. Smolentsev, A. Algasov, O. Usoltsev, M. Soldatov, A. Bugaev, Y. Rusalev, C. Lamberti and A. Soldatov, *Comput. Phys. Comm.*, 2019, 107064.

[8] A. Martini, A. A. Guda, S. A. Guda, A. Dulina, F. Tavani, P. D'Angelo, E. Borfecchia and A. Soldatov, *Phys. Conf. Series*, 2020, submitted.

[9] I. Markovsky, *Automatica*, 2008, **44**, 891–909.

[10] J.-U. Rohde, S. Torelli, X. Shan, M. H. Lim, E. J. Klinker, J. Kaizer, K. Chen, W. Nam and L. Que, *J. Am. Chem. Soc.*, 2004, **126**, 16750–16761.

[11] P. Chandrasekaran, S. C. E. Stieber, T. J. Collins, L. Que, Jr., F. Neese and S. DeBeer, *Dalton Trans.*, 2011, **40**, 11070–11079.

[12] M. Benfatto and S. Della Longa, *J. Synchr. Rad.*, 2001, **8**, 1087–1094.

[13] M. Benfatto, S. Della Longa and C. R. Natoli, *J. Synchr. Rad.*, 2003, **10**, 51–57.

[14] F. Tavani, A. Martini, G. Capocasa, S. Di Stefano, O. Lanzalunga and P. D'Angelo, *Inorg. Chem.*, 2020, **59**, 9979–9989.

[15] P. D'Angelo, A. Zitolo, G. Aquilanti and V. Migliorati, *J. Phys. Chem. B*, 2013, **117**, 12516–12524.

[16] E. Burattini, P. D'Angelo, A. Di Cicco, A. Filipponi and N. V. Pavel, *J. Phys. Chem.*, 1993, **97**, 5486–5494.

[17] K. Hayakawa, K. Hatada, P. D'Angelo, S. Della Longa, C. Natoli and M. Benfatto, *J. Am. Chem. Soc.*, 2005, **126**, 15618–23.

[18] P. D'Angelo and V. Migliorati, *J. Phys. Chem. B*, 2015, **119**, 4061–4067.

[19] G. Roelfes, M. Lubben, K. Chen, R. Y. N. Ho, A. Meetsma, S. Genseberger, R. M. Hermant, R. Hage, S. K. Mandal, V. G. Young, Y. Zang, H. Kooijman, A. L. Spek, L. Que and B. L. Feringa, *Inorg. Chem.*, 1999, **38**, 1929–1936.

[20] E. J. Klinker, J. Kaizer, W. W. Brennessel, N. L. Woodrum, C. J. Cramer and L. Que Jr., *Angew. Chem. Int. Ed.*, 2005, **44**, 3690–3694.

[21] P. Virtanen, R. Gommers, T. E. Oliphant, M. Haberland, T. Reddy, D. Cournapeau, E. Burovski, P. Peterson, W. Weckesser, J. Bright, S. J. van der Walt, M. Brett, J. Wilson, K. Jarrod Millman, N. Mayorov, A. R. J. Nelson, E. Jones, R. Kern, E. Larson, C. Carey, İ. Polat, Y. Feng, E. W. Moore, J. Vand erPlas, D. Laxalde, J. Perktold, R. Cimrman, I. Henriksen, E. A. Quintero, C. R. Harris, A. M. Archibald, A. H. Ribeiro, F. Pedregosa, P. van Mulbregt and S. . . Contributors, *Nat. Methods*, 2020, **17**, 261–272.